Available online at www.sciencedirect.com
SCIENCE DIRECT®
Surface Science 560 (2004) 103–120
SURFACE SCIENCE
www.elsevier.com/locate/susc

Structure, bonding, and adhesion at the ZrC(1 0 0)/Fe(1 1 0) interface from first principles ☆

A. Arya [1], Emily A. Carter *

Department of Chemistry and Biochemistry, University of California, Box 951569, Los Angeles, CA 90095-1569, USA

Received 30 October 2003; accepted for publication 16 April 2004
Available online 4 May 2004

Abstract

We report a pseudopotential-based density functional theory (DFT) investigation of the interface between ZrC and bcc Fe. ZrC is a potential candidate for a protective coating for ferritic steels because of its favorable physical, chemical, and mechanical properties. Here we predict the atomic structure, bonding, and ideal work of adhesion (W_{ad}^{ideal}) of the interface formed between the most stable surfaces of ZrC and bcc Fe, namely, the ZrC(1 0 0)/Fe(1 1 0) interface. Bulk properties of ZrC and bcc Fe, calculated for calibration of the DFT approximations involved, are in good agreement with experiment. Further, all the low-index surfaces of ZrC and bcc Fe are observed to retain near ideal bulk termination, as observed experimentally. Stabilities of both ZrC and bcc Fe surfaces follow their respective packing density sequence, i.e., (1 1 0) < (1 1 1) < (1 0 0) for ZrC and (1 1 1) < (1 0 0) < (1 1 0) for bcc Fe. Based on surface energy values, we estimate that the critical stress required for crack propagation in bcc Fe to be at least 30% larger than in ZrC. The ZrC(1 0 0)/Fe(1 1 0) interface is well lattice-matched (≈1.7% strain) producing a fairly smooth interface with little structural relaxation. Bonding at the interface consists of covalent C p–Fe d mixing and some metallic Zr d–Fe d interactions. As the coating grows, decreases in inter-metallic bonding, coupled with increased intraceramic interactions, weaken the interfacial bonding. While a monolayer of ZrC is tightly bound to an Fe substrate ($W_{ideal} = 3.05$ J/m^2), the adhesion decreases upon film thickening, with the asymptotic value of W_{ad}^{ideal} reached for 4 ML of ZrC (~2.3 J/m^2). This interface strength is sufficiently high that it may survive as a coating for steels in extreme environments, though it is much smaller than the minimum energy required for fracture of either ZrC or Fe.

Keywords: Ceramic thin films; Carbides; Ceramics; Iron; Surface electronic phenomena (work function, surface potential, surface states, etc.); Adhesion; Coatings; Interface states; Low index single crystal surfaces; Surface relaxation and reconstruction

☆ This work was supported by the Army Research Office. A Department of Defense University Research Instrumentation Program grant via the Army Research Office provided computers on which many of the calculations were performed. Part of the computational work was also performed on SGI2000 machines available at NCSA at the University of Illinois.

* Corresponding author. Tel.: +1-3102065118; fax: +1-3102670319.
E-mail addresses: aarya@apsara.barc.ernet.in (A. Arya), eac@chem.ucla.edu (E.A. Carter).
[1] Present address: Bhabha Atomic Research Center, Materials Science, Division, Modular Labs, Mumbai 400 085, India.

0039-6028/$ - see front matter
doi:10.1016/j.susc.2004.04.022

1. Introduction

We recently characterized via DFT a hetero-epitaxial coating of TiC on a bcc Fe substrate [1]. The goal of the work was to assess the prospects of TiC for use as an alternative protective coating for ferritic steels. These steels are used extensively in several industrial and technological applications [2,3], e.g., pressure vessel and tubing, oil and gas pipe lines, transmission towers, gun barrels, etc. The conventional chrome coating on these ferritic steels has inherent microcracks formed during the electrodeposition process. Under severe operating conditions, these microcracks open up and allow diffusion of reactive/corrosive gases to the base metal. This leads to materials degradation via compound formation, melting, etc., thereby limiting the lifetime of the component [2,3]. Therefore, there is a strong motivation to search for alternative coatings which can survive high amplitude thermal and mechanical fluctuations and can protect steel against reactive/corrosive gas environments. In this respect, ceramics can be ideal candidates owing to unusual combinations of physical, chemical, and mechanical properties exhibited by them, e.g., high melting points, high hardness and stiffness, and good corrosion and oxidation resistance [2–4]. Particularly for ferritic steels, TiC, ZrC, and c-BN were envisioned as possible alternative coating materials because of their favorable mechanical and thermodynamic properties vis-à-vis those of steels [5–10]. These ceramics have melting points above 3000 °C, their thermal conductivities are much lower than that of the conventional chrome coating, the coefficients of thermal expansion are comparable to that of steels, and their lattice mismatches with bcc Fe, in some specific orientations, are less than 3%, i.e., they may form coherent interfaces. Our earlier investigation of TiC's potential for coating [1] revealed a strong covalent-metallic bonding at the TiC/Fe interface with a reasonably high value of the ideal work of adhesion. That work motivated the exploration of isostructural ZrC for its possible use as an alternative protective coating for steels.

In this paper, we focus our attention on the interface formed between most stable surfaces of bcc Fe and ZrC, i.e., the ZrC(1 0 0)/bcc Fe(1 1 0) interface. The present pseudopotential-based DFT calculations have been carried out to understand the atomic and electronic structure, nature of bonding, and adhesion at this interface. This work forms the next phase of our search of a suitable alternative coating, following our earlier investigation of the TiC(1 0 0)/Fe(1 1 0) interface [1]. Our methodology, too, remains more or less the same as employed for the TiC coating, i.e., we start with an understanding of the nature of bonding operative in the bulk phase and characterize the change in the electronic structure as one goes from the bulk to the surface and finally to the interface [11,12]. Such bulk and surface calculations also provide useful calibrations of the approximations inherent in any implementation of DFT. In this paper, we will not discuss our results for bcc Fe and its surfaces, which have already been reported elsewhere [1]. Instead, we reproduce, wherever necessary, those results to augment our understanding of interfacial interactions.

ZrC, like other refractory transition metal carbides, has been studied extensively using experimental techniques [13–16], e.g., valence band photoemission, X-ray emission, optical spectroscopy, etc., as well as theoretical tools such as all-electron 3-D periodic DFT, e.g., the augmented plane wave (APW) method [17], muffin-tin orbital (MTO) techniques [18] and their linearized versions, LAPW and LMTO [19]. Several reviews of experimental and theoretical findings for metal carbides and nitrides are available [4,20–22]. These studies have established that ZrC, like other transition metal carbides, exhibits exceptional multifunctional properties due to a mixture of ionic, covalent and metallic bonding that are present simultaneously in its NaCl-type crystal structure [4,14,15]. The non-metal (C p)–metal (Zr d) covalent bonding dominates over metal–metal bonding and significant charge transfer from the metal to non-metal atoms occurs. The local density approximation (LDA) band structures obtained using APW and LAPW methods [4,21] for ZrC also compare well with experiments obtained using both angle-resolved photoemission [23], and *k*-resolved inverse photoemission [24] techniques. We shall see that our pseudopotential-based DFT predictions of bonding in ZrC agree well with the above findings.

The low-index surfaces of ZrC have been studied experimentally by several workers (for a review, see [25,26]). To the best of our knowledge, no theoretical results have been reported on ZrC surfaces so far. The (1 0 0) surface has been studied experimentally using inverse photoemission spectroscopy [27] to determine surface-induced states and surface shifts in core electron binding energies. Chemical shifts in core-level binding energies have been utilized to investigate the extent of charge transfer in these compounds. Similarly, the ZrC(1 1 1) surface was studied using impact collision ion scattering spectroscopy (ICISS) [28] to determine the structure of the surface, which exhibited a distinct 1×1 low-energy electron diffraction (LEED) pattern, indicating no surface reconstructions or signs of facets or superstructures. The ICISS data indicated a preferential metal termination for the (1 1 1) surface, while the subsurface layers are composed of alternating layers of metal and non-metal atoms [29–31]. As shown below, our pseudopotential-based DFT results agree with these measurements, where we observe only small structural relaxations for low-index surfaces of ZrC and a preference for the (1 1 1) surface to be metal-terminated.

Earlier theoretical investigations of interfaces involving transition metal carbides focused on correlating wetting behavior with electronic properties of various carbides (see Ref. [32]). These studies concluded that the more stable the carbide, the smaller the wettability, based on an observed linear dependence of the work of adhesion on the shift in energy of C 1s electrons. More recently, Dudiy et al. [33,34] examined Co(0 0 1)/TiX(0 0 1) interfaces (X = C,N) using plane wave pseudopotential DFT within the generalized gradient approximation (GGA; PW91 [35]) to exchange and correlation. They observed that the interfacial bonding mainly consists of a strong covalent Co 3d and C(N) 2p interaction, with Co/TiC exhibiting stronger adhesion than Co/TiN. Christensen et al. [36] used DFT-GGA to compare Co/TiC and Co/WC interface adhesions, where WC was found to produce the strongest interface, due to significant Co–W metallic bonding. To the best of our knowledge, no theoretical study of ZrC/Fe interfaces has been reported. Our investigation of the TiC/Fe interface [1] indicated strong covalent bonding between Fe and C, with somewhat weaker but still significant Fe–Ti metallic bonding. We expect similar bonding character to be present at the ZrC/Fe interface, due to Ti and Zr being isoelectronic; however, the larger Zr 4d orbitals may lead to subtle changes in properties that we now explore. We shall see that the size mismatch between Zr 4d and Fe 3d, compared to Ti 3d and Fe 3d, reduces the metal–metal bonding for ZrC on Fe.

Since we are considering ZrC as a possible coating for ferritic steels at elevated temperatures, it is of interest to evaluate the thermodynamic feasibility for formation of an unreacted Fe/ZrC interface vis-à-vis formation of Fe_3C and FeZr compounds at the interface. A rough estimate may be obtained from a thermodynamic analysis of bulk experimental data [37,38] at, e.g., 1000 K. The reactions

$$ZrC + Fe \rightarrow Fe_3C + Zr \quad \text{and}$$
$$ZrC + Fe \rightarrow FeZr + C$$

have free energy changes, ΔG, of +178.30 and +185.56 kJ/mol, respectively. [2] Thus it appears unlikely that compounds will form at interfaces between ZrC and Fe and we are safe to evaluate the stability of unreacted interfaces. Later, we will compare these values with Fe/ZrC interface energies obtained using DFT.

In this paper, we systematically investigate the electronic, structural, and bonding properties of the bulk and several low-index surfaces of ZrC and a ZrC(1 0 0)/bcc Fe(1 1 0) interface formed between most stable surfaces of Fe and ZrC. For our investigation, we examine up to four monolayer (ML) thick coatings of ZrC(1 0 0) on bcc Fe(1 1 0). In the next section, we briefly delineate the theoretical details used for calculations of bulk, surface, and interface properties. We then present analyses of the predicted electronic, structural, and

[2] From Refs. [37,38]: ΔG(ZrC,1000 K) = −188.00 kJ/mol; ΔG(C(gr), 1000 K) = −12.66 kJ/mol; ΔG(Zr(hcp), 1000 K) = −52.36 kJ/mol; ΔG(Fe(bcc), 1000 K) = −42.34 kJ/mol; ΔG(Fe_3C, 1000 K) = +0.31 kJ/mol; ΔG(FeZr, 1000 K) = −32.11 kJ/mol.

thermodynamic properties of the bulk phases and their surfaces. Lastly, predictions of atomic structure, bonding, and adhesion energetics of the interface are reported and prospects for ZrC as an alternative coating on steels are considered.

2. Theoretical method

Here we summarize only the key aspects of our calculational approach (for further details, see Ref. [1]). We performed pseudopotential plane-wave-based density functional theory (DFT) calculations, using both the local-density (LDA) and generalized gradient approximations (GGA) for the exchange-correlation potential, as parameterized by Perdew and Zunger [39] and Perdew and Wang [35], respectively. We used the "Vienna ab-initio simulation package" (VASP) [40], which solves the Kohn–Sham equations using a plane wave expansion for the valence electronic density and wave functions. The interactions between the ions and electrons are described by the Vanderbilt ultrasoft pseudopotentials (US-PPs) [41]. Non-linear partial core corrections to exchange and correlation were included for all species.

The salient features of our calculations are:

1. We carried out spin-restricted self-consistent calculations for bulk ZrC and its surfaces under both LDA and GGA, whereas spin-polarized GGA calculations were employed for bulk bcc Fe, its surfaces, and its interfaces with ZrC. Tests comparing results from spin-restricted versus spin-polarized calculations on pure ZrC revealed no essential differences in properties and therefore only the spin-restricted results are reported here for pure ZrC.
2. Our calculations are fully converged with respect to the size of the basis set (kinetic energy cutoff (E_{cutoff})), the number of **k**-points ($N_{\mathbf{k}}$), slab thickness (t_{slab}), and vacuum thickness (t_{vac}) (see Table 1).
3. The non-local US-PPs used in this study are those provided in VASP database (version 4.4). The atomic ground state electronic configurations for which the respective pseudopotentials were constructed are non-magnetic d^3s^1, s^2p^2, and d^7s^1 for Zr, C, and Fe, respectively. For Zr, we used US-PPs with explicit 4p semi-core states, whereas for carbon, we used the softer (i.e., lower default energy cutoff, E_{cutoff}) version of the pseudopotential. These US-PPs for Zr and C were found to be more accurate energetically compared to the corresponding standard US-PPs taken even at higher E_{cutoff}. For ZrC, Zr, and C LDA US-PPs were used for LDA calculations, whereas GGA USPPs were used in all GGA calculations. For Fe, we always used the GGA US-PP, since all calculations involving Fe were performed using the GGA.
4. For Brillouin zone integration, we employed the first-order Methfessel–Paxton smearing scheme [42] using a smearing width of 0.1 eV, resulting in a very small entropy term (<0.5 meV/atom) in all cases.
5. For surfaces and interfaces, we used periodic supercells containing a finite slab and a vacuum layer. We employed a 1×1 surface geometry for all surface slabs (Fig. 1), since no surface reconstructions are observed [25,26,28]. For ZrC(1 0 0) and ZrC(1 1 0), each layer contains one Zr and one C atom. For polar ZrC(1 1 1), each layer contains either Zr or C atoms (Table 1). DFT calculations were performed for the stoichiometric ZrC(1 1 1) surface having equal numbers of Zr- and C-layers, as well as the non-stoichiometric ZrC(1 1 1) surface, where the slab was terminated on both sides by a Zr-layer, consistent with experimental observations of a metal-terminated surface. We report results of metal-terminated ZrC(1 1 1) surface only, since it was found to be energetically more favorable, based on a comparison of slab cohesive energies.
6. For the interface calculations, the equilibrium bulk lattice vectors for bcc Fe(1 1 0) were employed to mimic heteroepitaxial growth of ZrC on a bcc Fe(1 1 0) substrate. This corresponds to an average lattice mismatch of 1.7%, with ZrC slightly expanded when adsorbed on Fe(1 1 0). The surface lattice vectors selected were [6 3 0] and [2 0 0], respectively, along **a** and **b** for the Fe substrate and [4 1 −1] and [1 1 −1], respectively, along **a** and **b** for the

Table 1
Converged parameters used for DFT calculations on bulk hcp Zr, graphite C, ZrC, and bcc Fe, their surfaces, and interfaces

System	E_{cutoff} (eV)	$N_{\mathbf{k}}$ (Fourier grid)	t_{slab} (no. of layers) [N_A, N_B]	t_{vac} (Å)
Zr (hcp)	200.00 (149.93)	105 (13×13×9)	–	–
C (gr)	250 (211.29)	105 (13×13×9)	–	–
ZrC	275.00	120 (15×15×15)	– [1 (Zr), 1 (C)]	–
bcc Fe	300.0 (237.51)	120 (15×15×15)	– [1 (Fe)]	–
ZrC(1 0 0)	275.00	36 (15×15)	5 [5 (Zr), 5 (C)]	10
ZrC(1 1 1)	275.00	27 (15×15)	7 [4 (Zr), 3 (C)]	12
ZrC(1 1 0)	275.00	64 (15×15)	5 [5 (Zr), 5 (C)]	10
bcc Fe(1 1 0)	300.0	64 (15×15)	7 [7 (Fe)]	12
bcc Fe(1 0 0)	300.0	64 (15×15)	7 [7 (Fe)]	12
bcc Fe(1 1 1)	300.0	27 (15×15)	7 [7 (Fe)]	12
1 ML ZrC(1 0 0)/Fe(1 1 0)	300.0	36 (6×6)	5 (Fe) + 1 (ZrC) [3 (C), 3 (Zr), 30 (Fe)]	12
2 ML ZrC(1 0 0)/Fe(1 1 0)	300.0	36 (6×6)	5 (Fe) + 2 (ZrC) [6 (C), 6 (Zr), 30 (Fe)]	12
3 ML ZrC(1 0 0)/Fe(1 1 0)	300.0	36 (6×6)	5 (Fe) + 3 (ZrC) [9 (C), 9 (Zr), 30 (Fe)]	12
4 ML ZrC(1 0 0)/Fe(1 1 0)	300.0	36 (6×6)	5 (Fe) + 4 (ZrC) [12 (C), 12 (Zr), 30 (Fe)]	12

E_{cutoff}, $N_{\mathbf{k}}$, t_{slab} and t_{vac} are the kinetic energy cutoff for the plane wave basis, the number of irreducible **k**-points, and the thickness of the slab and the vacuum, respectively. The numbers given in parentheses in the second column are the default E_{cutoff} for the corresponding elements, as given in VASP database. N_A and N_B are number of atoms of types 'A' and 'B' contained in the bulk or slab unit cell.

ZrC(1 0 0) surface. The misfit was 3.9% and 1.8%, respectively, along the **a** and **b** directions. This interface supercell (Fig. 4) consists of five layers of the bcc Fe(1 1 0) substrate with six Fe atoms/layer; each monolayer of ZrC(1 0 0) contained three C and three Zr atoms/layer. A five-layer slab of bcc Fe(1 1 0) was found to be adequate to model the substrate here, as the surface energies were converged to ~10 meV/atom for a five-layer slab. Table 1 lists the total number of layers and atoms of each kind for all interface supercells considered. As determined from our surface calculations, we employed a vacuum thickness of 12 Å for each interface slab (Table 1).

7. We used the conjugate gradient method to relax the ions into their local minima. All ionic relaxations were performed by keeping unit cell shapes and volumes fixed to the equilibrium bulk structures predicted at the GGA or LDA level. Further, all the atoms in the slabs (both surface and interface) were allowed to relax

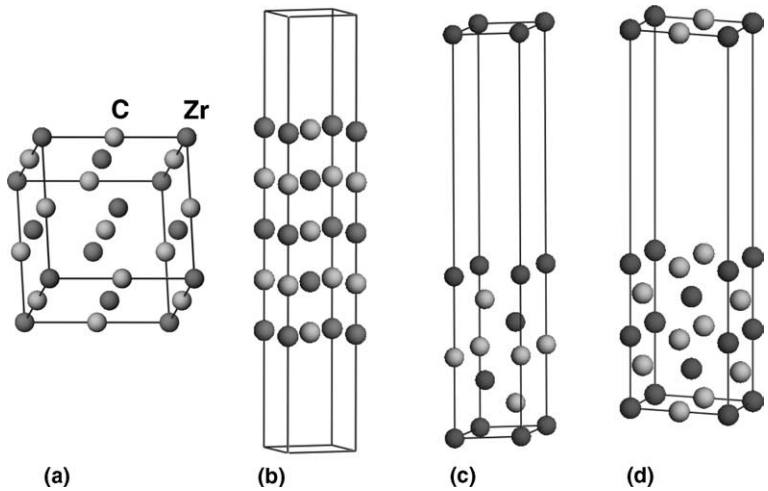

Fig. 1. (a) Bulk ZrC, and unrelaxed (b) ZrC(1 0 0), (c) ZrC(1 1 1), and (d) ZrC(1 1 0) surface slab unit cells used. The ZrC(1 0 0) and ZrC(1 1 0) slabs contained five layers with one Zr and one C atom in each layer. The ZrC(1 1 1) slab consisted of seven layers, alternating between pure Zr and pure C layers and is Zr-terminated at both surfaces. Here the dark grey spheres are Zr and the light grey spheres are C.

such that the residual force on each atom was less than 0.005 eV/Å.

8. The Wigner–Seitz (W–S) radii used for the calculation of partial density of states (PDOS) (*site*- and *l*-projected) were 1.666 Å for Zr, 1.191 Å for C, and 1.4095 Å for Fe. A volume-filling criterion was used to estimate the W–S radii. These W–S radii were chosen by scaling the elemental muffin-tin radii of the constituent elements to the compound in question such that a volume-filling criterion was fulfilled. The charge density plots include the full valence charge density, i.e., contributions from Zr 4p semi-core and augmentation charges are also accounted for.
9. For atomic calculations, the kinetic energy cutoffs for the plane wave basis (E_{cutoff}) were 275.0, 275.0, and 300 eV for isolated Zr, C, and Fe atoms, respectively. These E_{cutoff} values were sufficient to converge atomic energies to within 2 meV. Calculations on isolated atoms employed a cubic unit cell of length 10 Å, with partial occupancies fixed appropriately throughout.
10. For pure bulk Zr (hcp) and C (graphite) calculations, the W–S radii (1.76 Å for Zr and 1.15 Å for C) were chosen such that the spheres captured ~95% of the total charge density, although these radii are not volume filling.

3. Results and discussion

In this section, we present results of the calculations described above for bulk ZrC and its low-index surfaces, as well as for the ZrC(1 0 0)/bcc Fe(1 1 0) interface. As mentioned before, we do not discuss in detail the results for bcc Fe and its surfaces, which were thoroughly analyzed in our earlier publication on TiC/Fe interfaces [1].

3.1. ZrC bulk crystal and surfaces: structural, cohesive, and electronic properties

3.1.1. ZrC bulk properties

Table 2 displays predictions of equilibrium lattice parameters (a), bulk moduli (B_0), cohesive energies (E_{coh}), and formation energies (E_{form}). For bulk ZrC, we used both the LDA and GGA for electron exchange and correlation. For bcc Fe, we used only the spin-polarized GGA, as it is well known that LDA yields the incorrect ground state of bulk Fe [43]. For comparison, we also list available experimental values. ZrC, like TiC, has

Table 2
Comparison of USPP DFT LDA and GGA ground state properties of bulk ZrC with experiment

System	Lattice parameter (Å)	Bulk modulus (B_0) (GPa)	Cohesive energy (E_{coh}) (eV/ZrC formula-unit)	Formation energy (E_{form}) (eV/ZrC formula-unit)	DOS at ϵ_F ($\rho(\epsilon_F)$) (states/eV-cell)
USPP-LDA	4.644	241.8	18.338	−1.801	0.112
USPP-GGA	4.731	220.7	16.466	−1.835	0.129
Experiment	4.692–4.699[a]	168.2[b] 187.0[c] 220.0[d] 223.1[e] 227.9[f]	15.836[g]	−2.094[h]	

[a] Ref. [44].
[b] Ref. [46].
[c] Ref. [47].
[d] Ref. [8].
[e] Ref. [48].
[f] Ref. [49].
[g] Ref. [13].
[h] Ref. [10].

the NaCl (B1) structure in which the cations as well as the anions independently form fcc lattices and these two interpenetrating lattices are displaced from each other by $\mathbf{a}\langle\frac{1}{2}\,\frac{1}{2}\,\frac{1}{2}\rangle$ (see Fig. 1a). The equilibrium lattice parameter was calculated by minimizing the total energy ($E_T(V)$) with respect to volume (V). For ZrC, the GGA overestimates equilibrium lattice parameter by ~1% and the LDA underestimates it by the same amount compared with experiments [44]. The GGA yields a lattice constant for Fe in close agreement with experiment [1], and with previous theory.

The bulk modulus was obtained by fitting the $E_T - V$ data to the Murnaghan equation of state [45]:

$$E_T(V) = \frac{B_0 V}{B_0'}\left[\frac{(V_0/V)^{B_0'}}{B_0' - 1} + 1\right] + C$$

where B_0 is the bulk modulus, B_0' is the pressure derivative of B_0, V_0 is the equilibrium volume, and C is a constant. The GGA result for the bulk modulus of ZrC falls within the range of the experimental values [7,8,46–49], while the LDA value is at least ≈10% higher than observed, consistent with the usual LDA overbinding. The USPP GGA Fe bulk modulus is off by 6% from experiment (not shown) [1], but is consistent with earlier USPP-GGA values.

The cohesive energies (E_{coh}) in Table 2 were calculated from the difference in total energies between isolated atoms and the given (A_xB_y) compound. The DFT-GGA (LDA) value of E_{coh} for bulk ZrC output directly by VASP was 9.641 (10.547) eV/atom; however, this is with respect to the non-magnetic (NM) s^1d^3 and s^2p^2 reference configurations for Zr and C atoms, used to generate their associated pseudopotentials. The true ground states of Zr and C are high spin s^2d^2 (^{3}F) and s^2p^2 (^{3}P), respectively. Therefore, we calculated the energy difference ($\Delta E_{at} = E_{at}^{NM} - E_{at}^{gr.st.}$) in order to report cohesive energies referenced to the experimental ground states of the atoms. The GGA (LDA) values of ΔE_{at} for Zr and C atoms were 1.865 (1.845) and 0.950 (0.910) eV/atom, respectively. Accounting for ΔE_{at} yields the GGA (LDA) cohesive energy of ZrC as 8.233 (9.169) eV/atom or 16.466 (18.338) eV/ZrC formula-unit, which is higher than experiment by ≈0.6 eV/ZrC formula-unit. Part of this error is no doubt due to known systematic errors in the DFT energies of the isolated atoms (e.g., the self-interaction problem [50]). E_{coh} for bcc Fe (not shown) was calculated similarly, where we find that a proper accounting for the final state of the atom (i.e.

including ΔE_{at}) yields a GGA E_{coh} in quite good agreement with experiment [1].

Another means of estimating the stability of compounds that eliminates these systematic errors in the DFT description of the atoms is to calculate instead the energy of formation of the compound from the standard states of elements. This is given by $E_{form}(ZrC) = E_{coh}^{gr.st.}(Zr_{hcp}) + E_{coh}^{gr.st.}(C_{gr}) - E_{coh} \times (ZrC)$. Our DFT-GGA (LDA) cohesive energies for Zr (hcp) and C (graphite), properly referenced to the true atomic ground states, are 6.534 (7.372) and 8.097 (9.165) eV/atom, respectively. This yields GGA (LDA) formation energies that are lower than the experimental value by 12% (14%) [10]. The absolute LDA error is reduced considerably by examining E_{form} instead of E_{coh}, while the absolute GGA error is reduced only slightly.

ZrC exhibits a mixture of metallic, covalent, and ionic bonding. Its metallic nature can be seen (Table 2) in the finite density of states at the Fermi level ($\rho_{(E_F)}$). This can be observed also in the *site*- and *l*-projected PDOS for Zr and C in bulk ZrC (Fig. 2(a)). The covalent component of bonding can also be seen in the PDOS for bulk ZrC. Fig. 2(a) shows a low-lying C 2s band at $\sim$−9.5 eV, which is separated from the higher energy overlapping C 2p and Zr 4d bands by a gap of about 4 eV. This valence band exhibits a strong mixing of C 2p and Zr 4d that is responsible for covalent bonding in bulk ZrC. These findings are consistent with previous LDA calculations [4,21] on carbides of Ti, V, Zr, and Nb.

The ionic component of the bonding involves charge transfer from Zr to C, which is quantified Table 3. Our particular Wigner–Seitz radii suggest that Zr loses $\sim$0.12 e, while C appears to gain $\sim$0.27 e in ZrC compared to the pure elements. The inequality of these two estimates points to the limitations of such analysis and suggests we should simply regard these values as a possible range of a fairly small but non-zero charge transfer from Zr to C. These values are smaller than LDA values obtained by Neckel et al. [21] of 0.42 e. Other workers [4] have reported qualitatively similar charge transfer from metal to non-metal, irrespective of the radii of the Wigner–Seitz spheres. Of course, the arbitrary choice of Wigner–Seitz radii selected render these conclusions only qualitative in nature. A comparison of the *l*-decomposed charges between bulk ZrC and respective bulk elements (Table 3) qualitatively suggests that primarily Zr s electrons are donated to C p states, as also expected based on Zr ionization energies (IE): IE(Zr s) < IE(Zr d).

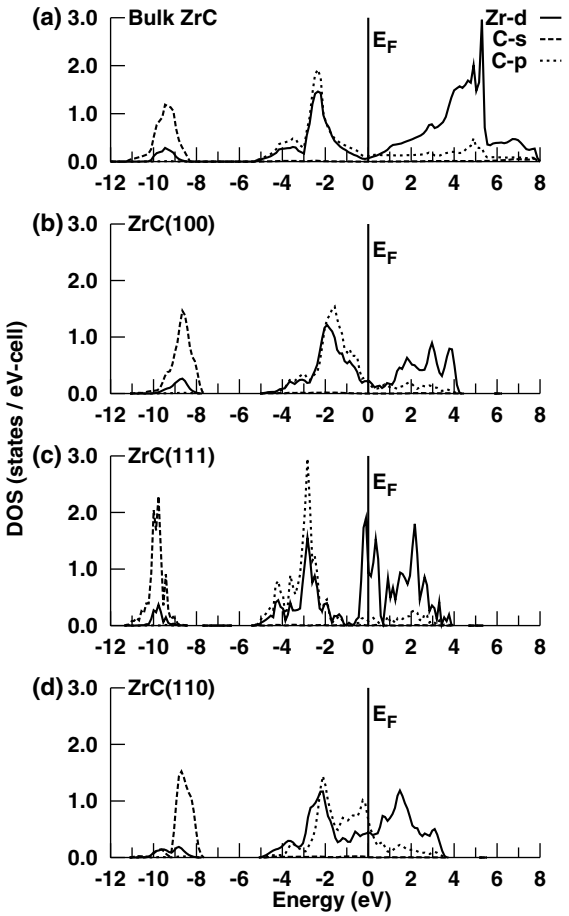

Fig. 2. The *site*- and *l*-projected partial density of states (PDOS) for (a) bulk ZrC, and the surface layer of (b) ZrC(1 0 0), (c) metal-terminated ZrC(1 1 1) (surface Zr and subsurface C), and (d) ZrC(1 1 0).

The valence charge distribution in the (1 0 0) plane of ZrC (Fig. 3(a)) also suggests this charge transfer from Zr to C, as evidenced by an almost spherically symmetric charge distribution around C atom because of the nearly half-filled 2p shell in $C^{\delta-}$. The partially filled Zr d band is responsible for non-sphericity of charge density around Zr

Table 3
Integrated electronic charges (Q_l) of C, Zr, ZrC, and Fe, partitioned according to angular momentum, for bulk, surface (S), and directly subsurface ($S-1$) atoms, inside their Wigner–Seitz spheres

System	C				Zr/Fe[a]				μ (μ_B/atom)
	Q_s	Q_p	Q_d	Q_T	Q_s	Q_p	Q_d	Q_T	
C (gr)[b]	1.420	2.142	0.270	3.832					–
Zr (hcp)[b]					0.558	6.383	2.350	9.291	–
ZrC	1.416	2.631	0.059	4.106	0.376	6.522	2.276	9.174	–
ZrC(1 0 0) – (S)	1.419	2.508	0.046	3.973	0.364	6.439	2.216	9.019	–
($S-1$)	1.414	2.675	0.061	4.150	0.381	6.530	2.275	9.185	
ZrC(1 1 1) – (S)[c]	–	–	–	–	0.407	6.352	2.289	9.049	–
($S-1$)	1.420	2.668	0.080	4.168	–	–	–	–	
ZrC(1 1 0) – (S)	1.438	2.394	0.044	3.876	0.376	6.350	2.313	9.039	–
($S-1$)	1.415	2.697	0.075	4.186	0.388	6.525	2.319	9.231	
Fe(1 1 0)									2.742
(S)(↑)					0.258	0.212	4.545	5.015	
(S)(↓)					0.260	0.227	1.786	2.273	

Q_T's are the total number of valence electrons inside the Wigner–Seitz spheres. The up and down arrows for bcc Fe surfaces indicate up-spin and down-spin components, respectively, and μ is the magnetic moment (in μ_B/atom) for Fe atoms at the surface.

[a] The Zr values include the 4p semi-core electrons.

[b] The Wigner–Seitz sphere radii selected for evaluation of partial charges for Zr (hcp) and C (gr) phases are 1.76 and 1.15 Å, respectively.

[c] There are no surface C atoms for the metal-terminated ZrC(1 1 1) surface.

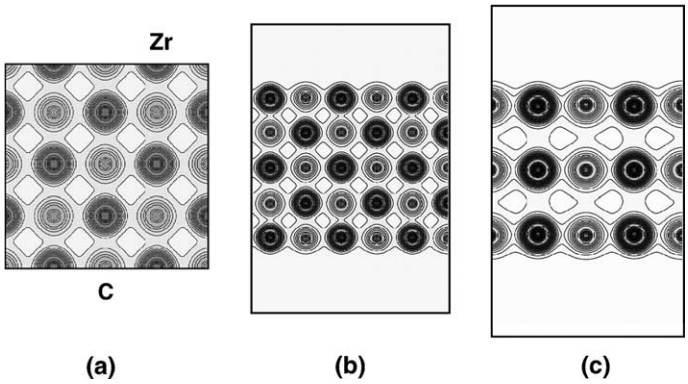

Fig. 3. Total valence charge density distributions on (a) the (0 0 1) plane of bulk ZrC, (b) the (0 1 1) plane of ZrC(1 0 0), and (c) the (0 0 1) plane of ZrC(1 1 0); each sliced through both Zr and C atoms. The charge concentration is proportional to the depicted intensity, with C having less charge around it and therefore appearing as a lighter grey. Note that the Zr density includes 4p semi-core electrons.

site, which is slightly polarized in the direction of the neighboring C atom.

3.1.2. ZrC surface properties

Here we present structural relaxations, electronic properties, e.g., surface DOS, surface-induced states, and charge transfer effects, etc., and surface energies of the (1 0 0), (1 1 1), and (1 1 0) surfaces of ZrC (Fig. 1(b)–(d)). As evident in Table 4, all surfaces of ZrC exhibit small inward structural relaxations, with Zr consistently moving inward slightly more than C. The degree of

Table 4
Vertical displacements (perpendicular to the surface), from bulk-terminated positions Δz (Å), upon relaxation of the surface (S) and the directly subsurface ($S-1$) atoms

System	Δz (Å)		$d^{p}_{\text{interlayer}}$ (Å)
	C	Zr	
ZrC(1 0 0)			
(S)	−0.006	−0.08	2.319 (2.366)
($S-1$)	0.021	−0.016	2.378 (2.366)
ZrC(1 1 1)			
(S)	–	−0.124	1.117 (1.366)
($S-1$)	0.125	–	1.541 (1.366)
ZrC(1 1 0)			
(S)	−0.075	−0.133	1.523 (1.673)
($S-1$)	0.070	0.023	1.719 (1.673)

Minus signs indicate movement into the bulk. $d^{p}_{\text{interlayer}}$ is interlayer distance between the layer (p) in question and the next layer below (see text). The values in parentheses are for the unrelaxed slabs.

relaxation increases as (1 0 0) < (1 1 1) < (1 1 0). The inter-layer spacing, $d^{p}_{\text{interface}}$, refers to the distance between the layer (p) in question and the next layer ($p-1$) below. The position of each layer is determined by taking an average of positions of the cation and the anion planes [54]. In ZrC(1 1 1) and ZrC(1 1 0), Zr and C atoms in the subsurface ($S-1$) layer move out towards the surface layer, thereby reducing the inter-layer separation. ZrC(1 1 0) exhibits the largest displacements of 0.133 and 0.075 Å, for the surface Zr and C atoms, respectively (Table 4), along with upward movement towards vacuum of the second layer atoms. This reduces the inter-layer separation between the surface and subsurface layers to 1.523 from 1.673 Å in the bulk-terminated surface. Similarly, in ZrC(1 1 1), the surface Zr atoms move into the bulk by 0.124 Å, while the directly subsurface C atoms move up toward vacuum by 0.125 Å upon relaxation, thereby reducing the inter-layer separation to 1.117 from 1.366 Å in the bulk-terminated surface. The ZrC(1 0 0) surface remains nearly bulk terminated. Moreover, we find no evidence for these low-index surfaces of ZrC to reconstruct, based on calculations using larger unit cells that would have allowed such reconstructions. Overall, the (1 0 0), (1 1 0), and (1 1 1) surfaces of ZrC show more or less an ideal bulk truncation, consistent with the 1×1 LEED patterns observed [25].

A comparison of *site*- and *l*-projected PDOS of bulk ZrC (Fig. 2(a)) and the surface layer of ZrC(1 0 0) (Fig. 2(b)) reveals that new states appear in the energy range between −4.0 and +4.0 eV around the Fermi level. The s-projected DOS for the Zr atom exhibits a negligibly small shift compared to d-projected DOS and hence it is not shown in Fig. 2. The C 2p and Zr 4d peaks in the occupied part of the DOS shift towards lower binding energy by about 0.8 eV, thereby reducing the valence band width and enhancing the degree of localization of electrons. Similarly, the low-lying C 2s peak is also shifted towards smaller binding energies by about 0.5 eV at the surface. The lower part of the C 2p band is markedly reduced in the surface layer, indicating that these states are sensitive to the formation of the surface. For both ZrC(1 1 1) and ZrC(1 1 0), the DOS at the Fermi level (Fig. 2(c) and (d)) is quite high and several new surface-induced states, arising from Zr d and C p electrons, are seen at the Fermi level. These states contribute to the instability of these surfaces as compared to ZrC(1 0 0). Further, the occupied part of valence band in the PDOS for ZrC(1 1 1) (Fig. 2(c)) shows a dip at around −1.0 eV separating the covalent Zr d–C p mixing region at higher binding energy and the totally Zr d-dominated region at the Fermi level, indicating the metallic character of the surface layer. By contrast, the PDOS for ZrC(1 1 0) exhibits primarily Zr d–C p covalent interactions (Fig. 2(d)).

The charges on the surface C atoms (Table 3) decrease going from bulk ZrC to ZrC(1 0 0) and finally to ZrC(1 1 0). Compared to C atoms in bulk ZrC, surface C atoms appear to lose 0.13 and 0.23 e at the (1 0 0) and (1 1 0) surfaces, respectively. This apparent reduction of charge is also evidenced by the valence charge distributions (Figs. 3(b) and (c)) in the (0 1 1) and (0 0 1) planes of ZrC(1 0 0) and ZrC(1 1 0), respectively, which show the reduction in sphericity for the surface C atoms as compared to the bulk. The reduction of charge at the surface may actually occur, or it can be that the electron density is simply distorted by the vacuum so that the integration within the W–S sphere is no longer accurate.

We may calculate the surface energy (E_{surf}) in a slab model as [1]:

$$E_{surf} = \frac{\left(E_{slab} - \left(\frac{N_{slab}}{N_{bulk}}\right)E_{bulk}\right)}{2A} \quad (1)$$

where E_{slab} and E_{bulk} are the total energies of the surface slab and the bulk unit cell, respectively. N_{slab} and N_{bulk} are the number of atoms contained in the slab and the bulk unit cells, respectively, and 'A' is the area of the surface unit cell. Table 5 displays DFT-GGA ZrC surface energies for both unrelaxed and relaxed structures; DFT-LDA surface energies are shown only for the most stable ZrC surface. As expected due to the typical LDA overbinding, the LDA surface energies are far too high. DFT-GGA yields a stability sequence for ZrC of (1 0 0) > (1 1 1) > (1 1 0), which correlates with their ideal packing densities (1.000:0.577:0.530 from $\frac{4}{a^2} : \frac{4}{a^2\cdot\sqrt{3}} : \frac{3}{a^2\cdot\sqrt{2}}$). The bcc Fe surface energies also follow their packing densities [1].

According to Griffith theory [55], the critical stress required for crack propagation in a brittle material (e.g., ZrC), with no plastic energy dissipation mechanisms, is roughly given by twice the surface energy. In ductile materials such as Fe, plasticity can dominate measurements of fracture energy. However, to a first approximation, the fracture energy may still be proportional to the surface energy in metals [55]. The DFT-GGA surface energies reported in Table 5 suggest that the critical stress required for crack propagation in bcc Fe along [1 1 0] is at least 30% larger than that in ZrC along [1 0 0]. Of course, plastic energy dissipation mechanisms available in Fe also favor cracking to occur in ZrC instead of Fe.

In sum, all the low-index surfaces of ZrC exhibit nearly ideal bulk termination. ZrC(1 0 0) and ZrC(1 1 0) show predominantly polar covalent bonding, while the metal-terminated ZrC(1 1 1) is a mixture of metallic and polar covalent bonding character at the surface. The stabilities of ZrC surfaces follow their packing density sequence, with (1 0 0) > (1 1 1) > (1 1 0).

3.2. ZrC(1 0 0)/Fe(1 1 0) interface

In this section, we describe the predicted structure, bonding, and adhesion at the ZrC(1 0 0)/Fe(1 1 0) interface, which is formed between the most stable surfaces of ZrC and bcc Fe (the interface likely to be preferred energetically [56]). Also, this interface is the least strained (lattice mismatch 1.7%) among all combinations considered of low-index surfaces of ZrC and bcc Fe.

We select surface lattice vectors of bcc Fe(1 1 0) and ZrC(1 0 0) that lead to maximum overlap between the two surfaces by calculating a geometric misfit parameter, ζ, defined as [56]

$$\zeta = 1 - \frac{2\Omega}{A_1 + A_2}, \quad (2)$$

Table 5
DFT-GGA surface energies (E_{surf}, mJ/m^2) for low-index surfaces (both unrelaxed and relaxed structures) of ZrC and bcc Fe

System	E_{surf} (unrelaxed) (mJ/m^2)	E_{surf} (relaxed) (mJ/m^2)	ΔE_{relax} (meV/formula unit)
ZrC(1 0 0)	1677 (2228)	1592 (2042)	23.7 (52.0)
ZrC(1 1 1)	2799	2428	69.1
ZrC(1 1 0)	3422	3199	88.0
bcc Fe(1 1 0)	2289	2288 2417–2475[a] 2430[b]	0.1

Values in parentheses are DFT-LDA results for the most stable surface of ZrC. ΔE_{relax} (meV/formula unit) is the change in energy upon relaxation.

[a] Experimental [51,52].

[b] FCD-LMTO (GGA) [53].

for several possible combinations of surface lattice vectors. Here, A_i and Ω are surface areas ($i =$ ZrC(1 1 0) and bcc Fe(1 1 0)) and overlap area, respectively. The best-matched interface corresponds to minimum ζ. This analysis of surface matching provided us with a practical interface unit cell having a supercell area of 34.77 Å^2 and a lattice mismatch of 1.7%. The specific lattice vectors chosen are given in Section 2, salient feature (6). Further, in order to achieve asymptotic values for the properties of the coating, we progressively increased the thickness of ZrC coating from 1 to 4 ML (see Fig. 4). Table 1 lists the total number of atoms of each type in each layer for these interface supercells.

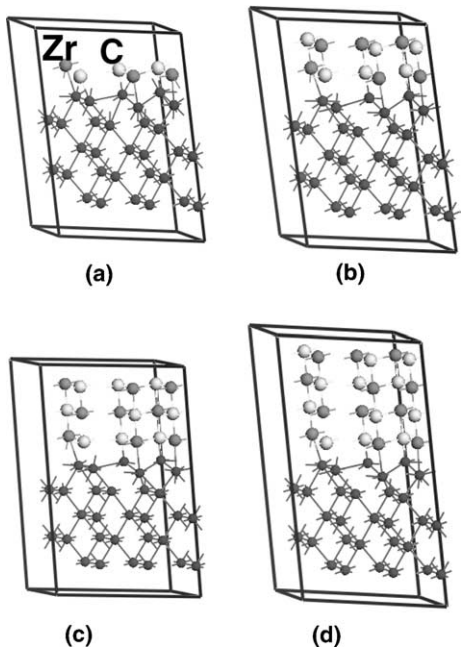

Fig. 4. Structurally relaxed ZrC(1 0 0)/Fe(1 1 0) interface slab unit cells for (a) 1 ML, (b) 2 ML, (c) 3 ML, and (d) 4 ML thick coatings of ZrC. The Fe substrate has five layers with six atoms per layer. Each ML of ZrC contains three atoms each of Zr (dark grey spheres) and C (light grey spheres).

3.2.1. Interface structure

Table 6 provides coordination numbers and nearest neighbor distances for atoms at or near the relaxed ZrC/Fe interface, as a function of ZrC coating thickness. The atoms are labelled according to their distance from the interface, e.g., Zr_1 is closer to the interface region than Zr_2, etc. The structure and bonding in the 3 and 4 ML ZrC coatings are similar, therefore we restrict our analysis here to ZrC coatings up to 3 ML thick. A comparison of various interatomic distances for the relaxed interface supercells and those in the bulk phases shows that these interfaces are more or less smooth with very little relaxation (Fig. 4).

For 1 ML of ZrC on Fe(1 1 0) (Fig. 4(a)), the minimum C–Fe distances are 2.02 and 2.15 Å for C_1 and C_2, respectively, and the minimum Fe–Zr bond lengths are 2.54 and 2.65 Å for Zr_1 and Zr_2, respectively. These values are very similar to the Fe–C distance in bulk Fe_3C (2.02 Å [44]), and the Fe–Zr distance in bulk FeZr (2.577 Å [44]), suggesting strong Fe–C and Fe–Zr interactions at the interface. In both the 2 and 3 ML ZrC films (Figs. 4(b) and (c)), the C_1 atom has five Zr atoms at distances ranging between 2.25 and 2.39 Å and one Fe atom at only ~2.00 Å away. Similarly, C_2 has five Zr atoms slightly further away on average (2.34–2.50 Å), while the C_2–Fe distances vary non-monotonically with coverage, with the longest distances (2.46–2.68 Å) seen in the 2 ML film. The C_3 atom has no direct C–Fe interactions, since it is in the second monolayer, but has near-bulk-like Zr–C bond lengths (2.31–2.37 Å). The Fe–Zr bond distances increase going from 1 to 2 ML, but the third ML of ZrC shortens some Zr–Fe bonds while lengthening others. The Fe_3 atoms, in the layer adjacent to the interface layer, have bonds of similar length to Zr and to other Fe atoms, suggesting significant metal–metal bonding across the interface, as we now examine.

3.2.2. Interface bonding

Fig. 5 displays *site*- and *l*-projected DOS for the atoms at and near the 1 ML ZrC/Fe interface. The covalent and metallic components of bonding across the interface come from a strong interaction between C_1 2p and Fe_1 d electrons, and somewhat weaker mixing of Zr_1 d–Fe_1 d states in the valence band (Fig. 5(a)). The higher coordination of Zr compared to C may compensate for the weaker Zr–Fe interaction, heightening the role of metal–metal bonding in the interface cohesion. One of

Table 6
Approximate number of nearest and next nearest neighbors (#nn) and their distance ranges (d_{nn} (Å), in parentheses) for atoms in the unit cell positioned at (subscript 1) and near (subscripts 2 and 3) the ZrC/Fe interface

System	Atom	#nn (d_{nn}, Å)		
		C	Zr	Fe
ZrC	C	–	6 (2.37)	
	Zr	6 (2.37)	–	
ZrC(1 0 0)	C_s		5 (2.37–2.38)	
	C_b		6 (2.35–2.37)	
	Zr_s	5 (2.26–2.37)		
	Zr_b	6 (2.37–2.39)		
bcc Fe(1 1 0)	Fe_s			2 (2.47) + 2 (2.86)
	Fe_b			4 (2.48) + 4 (2.86)
1 ML	C_1		4 (2.36–2.37)	1 (2.02)
ZrC(1 0 0)/Fe(1 1 0)	C_2		4 (2.39-2.42)	2 (2.15–2.16)
	Zr_1	4 (2.36–2.39)		1 (2.54)
	Zr_2	4 (2.37–2.42)		2 (2.65–2.66)
	Fe_1	1 (2.02)	1 (2.92)	3 (2.41–2.50) + 3 (2.59–2.74)
	Fe_2	1 (2.15)	1 (2.66)	6 (2.27–2.63)
2 ML	C_1		5 (2.25–2.39)	1 (2.00)
ZrC(1 0 0)/Fe(1 1 0)	C_2		5 (2.34–2.38)	2 (2.46–2.68)
	C_3		5 (2.31–2.37)	
	Zr_1	5 (2.31–2.39)		1 (2.73)
	Zr_2	5 (2.26–2.38)		2 (2.73–2.75)
	Zr_3	5 (2.25–2.37)		
	Fe_1	1 (2.00)	1 (2.99)	6 (2.43–2.76)
	Fe_2	1 (2.46)	1 (2.754)	1 (2.29) + 6 (2.44–2.69)
	Fe_3		1 (2.70)	7 (2.32–2.59)
3 ML	C_1		5 (2.34–2.38)	1 (1.99)
ZrC(1 0 0)/Fe(1 1 0)	C_2		5 (2.36–2.50)	2 (2.42–2.50)
	C_3		6 (2.28–2.37)	
	Zr_1	5 (2.33–2.39)		1 (2.73)
	Zr_2	5 (2.33–2.38)		1 (2.73) + 1 (3.01)
	Zr_3	6 (2.33–2.37)		
	Fe_1	1 (1.99)	4 (3.04–3.16)	7 (2.45–2.96)
	Fe_2	1 (2.42)	1 (2.74)	1 (2.28) + 7 (2.46–2.73)
	Fe_3		1 (2.73)	9 (2.31–2.73)

Bulk and surface atom coordination analyses for bulk ZrC, ZrC(1 0 0), and Fe(1 1 0) are also included for comparison. The subscripts 's' and 'b' refer to surface and bulk atoms, respectively. The coordination analysis of the 4 ML coating is similar to the 3 ML coating and hence is not shown.

the peaks in the C_1 PDOS (Fig. 5(a)) contributing to Fe–C bonding in the upper part of the valence band (at −1.0 eV) is diminished in the PDOS of C_2 and Fe_2 (Fig. 5(b)), and the C p PDOS for the β-states shift going from C_1 to C_2, such that the overlap of the Fe d and C p is greatly reduced. Both of these trends are consistent with diminished covalent bonding with increased bond distance. Examination of Tables 3 and 7 suggests that only small changes in electron distribution occur upon formation of the interface, where the carbon atoms gain only 0.01–0.04 e, the Fe atoms gain 0.14–0.23 e, and the Zr atoms lose 0.07 e, compared to isolated surfaces. Thus ionic bonding is not a significant contributor to the Fe–ZrC interface bonding in the 1 ML coating.

Since the PDOS of the 2 and 3 ML coatings are nearly identical, we only display (in Fig. 6) the

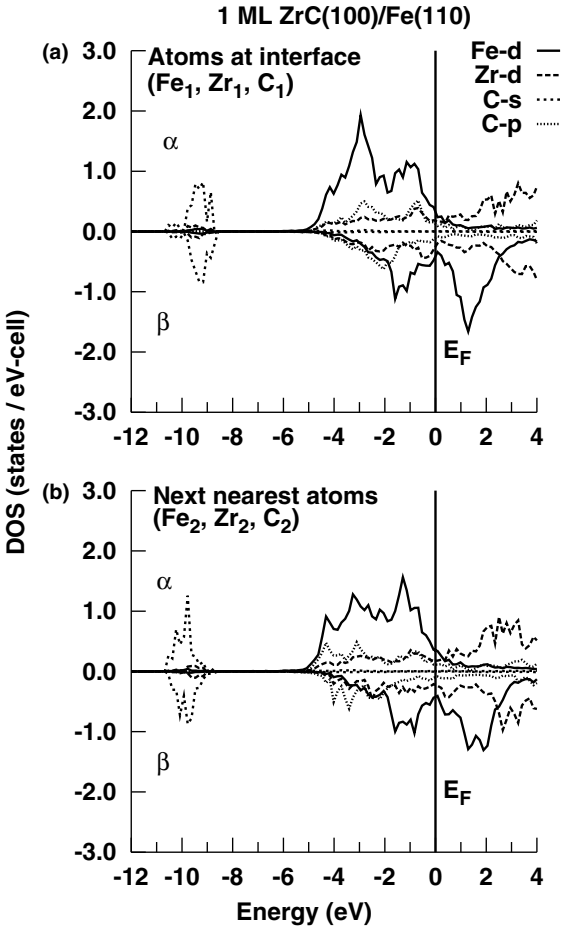

Fig. 5. Spin-polarized *site*- and *l*-projected PDOS for atoms (a) nearest, and (b) next nearest to the interface for 1 ML of ZrC on the bcc Fe(1 1 0) substrate. These atoms are designated with subscripts 1 and 2, respectively (see also Table 6). The α and β correspond to up and down spin PDOS, where the negative PDOS values simply refer to the PDOS of the down spin electrons. The same convention is used in Fig. 6.

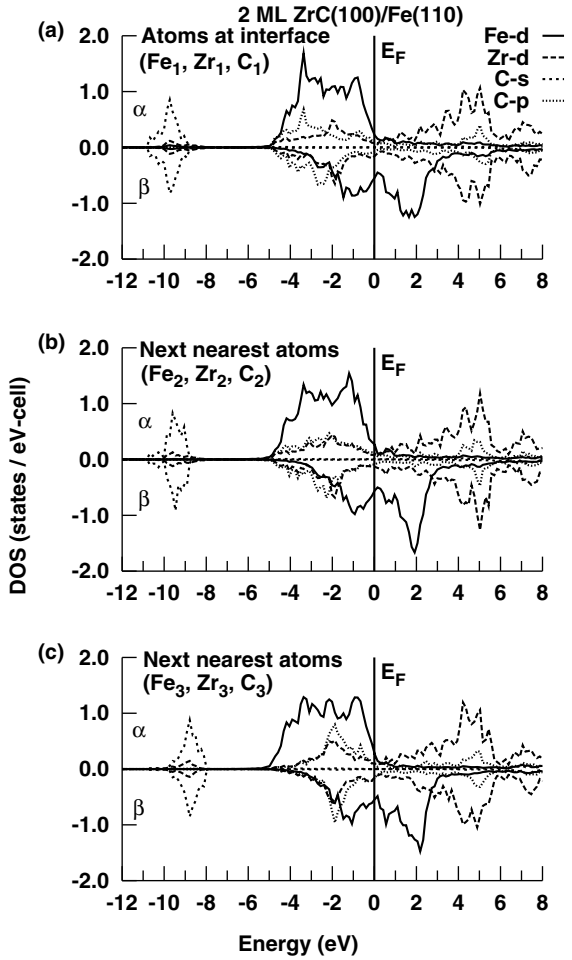

Fig. 6. Spin-polarized *site*- and *l*-projected PDOS for atoms (a) nearest, (b) second nearest, and (c) third nearest to the interface for 2 ML of ZrC on the Fe(1 1 0) substrate. These atoms are designated with subscripts 1, 2, and 3, respectively (see also Table 6).

PDOS for the 2 ML ZrC coating on Fe(1 1 0). The Zr_1 d peak shifts to higher binding energy as the coating thickens. Likewise, the interface C p peak (C_1) also shifts to higher binding energy, while C atoms further away shift to lower binding energy in the thicker film (towards bulk and isolated surface values). Fe–C PDOS overlaps are evident for all thicknesses of coatings, suggesting a fairly constant interaction. By contrast, the PDOS at the Fermi level shows reduced Fe d–Zr d interactions, as the PDOS here is dominated by Fe d states, with little participation from Zr_1 d states. An increase in Zr d–C p states overlap is evident, going from first- to third-nearest neighbors (Figs. 6(a)–(c)), indicating a progressive increase in intraceramic Zr–C covalent bonding as one moves away from the interface. Thus, reduced metallic Zr–Fe bonding and increased intraceramic bonding conspire together to weaken the interfacial bonding. As described below, this change in bonding correlates well with changes in the ideal work of adhesion as the coating grows.

Table 7
Spin-polarized integrated electronic charges (Q_l), partitioned according to angular momentum (l) inside Wigner-Seitz spheres, for atoms nearest (subscript 1) and next nearest (subscript 2) to the ZrC(1 0 0)/Fe(1 1 0) interface. Q_T's are the total number of valence electrons inside the Wigner–Seitz spheres

System		1 ML		2 ML		3 ML		4 ML	
		(↑)	(↓)	(↑)	(↓)	(↑)	(↓)	(↑)	(↓)
C_1	Q_s	0.708	0.709	0.707	0.709	0.709	0.711	0.708	0.711
	Q_p	1.266	1.263	1.334	1.348	1.308	1.329	1.301	1.333
	Q_d	0.035	0.029	0.043	0.038	0.044	0.038	0.045	0.038
	Q_T	2.010	2.001	2.084	2.094	2.061	2.078	2.053	2.081
	μ_a	0.009		−0.010		−0.017		−0.021	
C_2	Q_s	0.702	0.702	0.703	0.700	0.704	0.701	0.701	0.699
	Q_p	1.263	1.249	1.298	1.282	1.270	1.258	1.259	1.261
	Q_d	0.037	0.033	0.031	0.030	0.031	0.030	0.032	0.030
	Q_T	2.002	1.984	2.032	2.012	2.005	1.989	1.991	1.989
	μ_a	0.018		0.020		0.016		0.002	
Zr_1	Q_s	0.180	0.186	0.188	0.192	0.186	0.189	0.186	0.189
	Q_p	3.202	3.195	3.243	3.249	3.241	3.247	3.240	3.244
	Q_d	1.034	1.158	1.107	1.174	1.112	1.156	1.120	1.153
	Q_T	4.415	4.538	4.538	4.616	4.540	4.592	4.547	4.586
	μ_a	−0.123		−0.078		−0.052		−0.039	
Zr_2	Q_s	0.177	0.191	0.199	0.204	0.187	0.190	0.196	0.200
	Q_p	3.182	3.176	3.262	3.269	3.242	3.247	3.253	3.261
	Q_d	1.034	1.142	1.153	1.190	1.115	1.153	1.155	1.176
	Q_T	4.393	4.510	4.614	4.662	4.544	4.590	4.605	4.638
	μ_a	−0.117		−0.048		−0.046		−0.033	
Fe_1	Q_s	0.253	0.249	0.246	0.245	0.253	0.252	0.246	0.246
	Q_p	0.275	0.304	0.270	0.298	0.291	0.315	0.272	0.298
	Q_d	4.413	1.935	4.421	1.921	4.372	2.016	4.403	1.956
	Q_T	4.941	2.487	4.936	2.464	4.916	2.583	4.921	2.500
	μ_a	2.454		2.472		2.333		2.421	
Fe_2	Q_s	0.257	0.261	0.246	0.253	0.244	0.243	0.248	0.255
	Q_p	0.282	0.326	0.247	0.285	0.271	0.294	0.257	0.291
	Q_d	4.373	2.016	4.475	1.865	4.416	1.929	4.461	1.899
	Q_T	4.912	2.604	4.969	2.400	4.931	2.467	4.965	2.446
	μ_a	2.308		2.558		2.464		2.519	

μ_a (μ_B) are the atom-resolved magnetic moments.

Table 7 shows an increase in total electron charge on interfacial Zr (a gain of 0.20 e) and C (a gain of 0.17 e) atoms going from 1 to 2 ML coatings, but with no further increase for the C atoms going from 2 to 3 ML ZrC. The Zr atoms continue to draw slightly more charge going from 2 to 3 ML ZrC. This is yet another indication of increased intraceramic Zr–C bonding, as these charges approach that seen in bulk ZrC as the film thickens. The total charge on the interface Fe atoms changes little with coating thickness, while the magnetic moment of the interface Fe atoms is slightly higher than the bulk value ($2.33\mu_B$) for most coating thicknesses. The Fe atoms at the interface induce a small magnetization in the Zr atoms for the monolayer coating, but this magnetization is quenched as the film thickens. This again suggests reduced Fe–Zr interactions as the film grows.

3.2.3. Interface adhesion

The ideal work of adhesion, W_{ad}^{ideal}, is the energy required (per unit area) to reversibly separate a material into two free surfaces, ignoring plasticity.

W_{ad}^{ideal} can be calculated either using the difference between surface and interface energies or from the difference in total energies between the interface and its isolated components (in this case, substrate and coating):

$$W_{ad}^{ideal} = \sigma_{1v} + \sigma_{2v} - \sigma_{12} = \frac{E^{substrate} + E^{coating} - E^{interface}}{A}, \quad (3)$$

where σ_{iv} is the surface energy per unit area of the ith slab, σ_{12} is the interface free energy per unit area, A is the interface area, and $E^{substrate}$, $E^{coating}$, and $E^{interface}$ are the total energies of the isolated substrate, the isolated coating, and the interface, respectively. Attractive interactions between the two surfaces corresponds to $W_{ad} > 0$. The second identity in Eq. (3) is used here to calculate W_{ad}^{ideal} for ZrC coatings on a Fe substrate. The energy of the isolated coating was calculated using the same lattice vectors as for the interface, to cancel the effect of lattice mismatch strain. As mentioned earlier, all the atoms in the interface slab were allowed to relax. Our predictions are, of course, lower bounds for the work of adhesion obtained by experiment, as the energy required in reality is always greater than W_{ad}^{ideal} (because of dissipative plastic and diffusional processes).

Our DFT-GGA calculations predict W_{ad}^{ideal} for the fully relaxed interfaces to be 3.05, 2.12, 2.26, and 2.31 J/m^2 for the 1, 2, 3, and 4 ML thick coatings of ZrC on bcc Fe, respectively. Thus, the bonding of a single ZrC layer to an Fe substrate is considerably stronger than that for 2, 3, or 4 ML thick ZrC coatings. These results are similar to our earlier work for TiC coatings on Fe [1] and ZrO_2 coatings on Ni [11]. W_{ad}^{ideal} then drops precipitously at 2 ML and above, oscillating around ~2.3 J/m^2. This observed trend in W_{ad}^{ideal} conforms with the electronic properties of these ZrC coatings discussed earlier, where we observed a decrease in interfacial bonding at the expense of intraceramic bonding going from 1 to 2 or more ML. Intraceramic bonding reaches its saturation (bulk-like) character for a 3 ML coating, where the ideal work of adhesion has almost attained its asymptotic value. This asymptotic value for W_{ad}^{ideal} corresponds to −40.1 kJ/mol as the energy of formation of an interface, i.e., the adhesion process: ZrC (coating) + Fe (substrate) → Fe/ZrC (interface) is predicted to be exothermic at 0 K. Compared with the highly endoergic free energies of formation of FeZr and Fe_3C at 1000 K (see Section 1), the formation of an unreacted interface appears dramatically more favorable thermodynamically.

Comparing the ideal interface strength of ZrC/Fe with the energy required to form two surfaces of ZrC(1 0 0) (3184 mJ/m^2) or of Fe(1 1 0) (4576 mJ/m^2), reveals that the heterogeneous interface will be the weak link in the material. However, this interface strength is predicted to be comparable to that of the TiC/Fe interface studied earlier [1], which had an asymptotic value for W_{ad}^{ideal} of ~2.6 J/m^2. We observe stronger Fe–Ti interactions across the interface for TiC/Fe than for ZrC/Fe. The metal–metal bonding component is likely the reason for the enhanced W_{ad}^{ideal} for TiC/Fe. However, ZrC, like TiC, may still be practical as an alternative coating on steel due to the strong covalent and some metallic bonding that exists across the interface, its lower lattice mismatch with Fe compared to TiC, along with a fairly high W_{ad}^{ideal}. Moreover, other desirable properties of ZrC, e.g., its high melting point, hardness, and wear resistance, etc., may allow such a coating to survive in extreme environments.

4. Summary

We employed a pseudopotential-based DFT-GGA method to study bulk ZrC and its low-index surfaces, as well as a ZrC/Fe interface. The objective was to investigate the possibility of using ZrC as an alternative protective coating for ferritic steels. Earlier, we studied the TiC/Fe interface [1] with the same goal in mind, where we concluded that TiC could potentially replace the conventional Cr coating because of strong TiC/Fe interfacial bonding and a correspondingly high value for its ideal work of adhesion. The isostructural ZrC also exhibits favorable mechanical and thermodynamic properties as required for strong adhesion to steels, and an even lower lattice mismatch with Fe than exhibited by TiC.

We selected the ZrC(1 0 0)/Fe(1 1 0) interface, formed between the most stable surfaces of ZrC and bcc Fe, in order to study the nature of bonding at the interface and to predict its ideal work of adhesion. We studied up to 4 ML thick coatings of ZrC on a bcc Fe substrate. This interface has a low lattice mismatch of only ~1.7%. The predicted bulk cohesive and electronic properties of ZrC and bcc Fe, as well as the qualitative features of the structures of low-index surfaces of ZrC and Fe (i.e., negligible surface relaxation), agree well with experiment. ZrC(1 0 0) and Fe(1 1 0) were determined to be the most stable, while ZrC(1 1 0) and Fe(1 1 1) were the least stable, with the stability of these surfaces correlating with packing density. ZrC surfaces exhibited predominantly polar covalent character arising from Zr d–C p mixing. The metal-terminated ZrC(1 1 1) surface exhibited a mixture of polar covalent and metallic Zr d–d bonding. The critical stress required for crack propagation in bcc Fe was estimated to be at least 30% larger than that in ZrC, suggesting cracks will form in ZrC before they will form in Fe.

The nature of interfacial interactions for ZrC coatings is quite similar to that observed for TiC coatings [1], though the intermetallic bonding is stronger in the latter case, perhaps due to a better orbital size matching between Ti and Fe compared to Zr and Fe. A mixture of covalent and metallic bonding, due to Fe d–C p and Fe d–Zr d interactions, respectively, was found to exist at the interface. Ionic interactions were negligible for all coating thicknesses. The equilibrium Fe–C and Fe–Zr nearest neighbor distances for the 1 ML coating are nearly the same as those in bulk Fe_3C and in FeZr, suggesting strong Fe–C and Fe–Zr bonding for this ultrathin film. As the coating thickness increases, the intraceramic (polar covalent Zr–C) bonding component progressively increases, with a concomitant fall in Fe–Zr metallic bonding. This decreases the strength of the interface as the coating thickens. The intraceramic bonding reaches a saturation level for a 3–4 ML coating of ZrC. This is reflected in the W_{ad}^{ideal} values for these interfaces, which drops from 3.05 J/m^2 for 1 ML ZrC to 2.12, 2.26, and 2.31 J/m^2 for the 2, 3, and 4 ML films, due to the increase in intraceramic bonding at the expense of interfacial bonding.

The interfacial adhesion strength of a ZrC coating on Fe, as determined by the nature of bonding and quantified by W_{ad}^{ideal}, is reasonably high. This suggests that ZrC, like TiC, might be useful as an alternative, environmentally friendly protective coating for ferritic steels operating in harsh environments.

References

[1] A. Arya, E.A. Carter, J. Chem. Phys. 118 (2003) 8982.
[2] F.B. Pickering, in: R.W. Cahn, P. Haasen, E.J. Kramer, F.B. Pickering (Eds.), Materials Science and Technology, vol. 7, VCH, New York, 1992, p. 335.
[3] J.E. Truman, in: R.W. Cahn, P. Haasen, E.J. Kramer, F.B. Pickering (Eds.), Materials Science and Technology, vol. 7, VCH, New York, 1992, p. 527.
[4] K. Schwarz, CRC Crit. Rev. Solid State Mater. Sci. 13 (1987) 11, and references therein.
[5] E. Lang (Ed.), Proceedings of Coatings for High Temperature Applications, Elesevier Applied Science Publishers, London, 1983.
[6] R. Freer, The Physics and Chemistry of Carbides, Nitrides and Borides, NATO ASI Series E: Applied Sciences, vol. 185, 1989.
[7] ASM Engineering Materials Reference Book, ASM International, Metals Park, Ohio, 1989.
[8] E.A. Brandes, G.B. Book (Eds.), Smithells Metals Reference Book, Butterworth-Heinemann, Oxford, 1998.
[9] J.F. Shackleford, W. Alexander, J.S. Park (Eds.), CRC Materials Science and Engineering Handbook, CRC Press, Boca Raton, 1994.
[10] I. Barin, O. Knacke, O. Kubaschewski, Thermochemical Properties of Inorganic Substances, Springer, Berlin, 1989.
[11] A. Christensen, E.A. Carter, J. Chem. Phys. 114 (2001) 5816.
[12] A. Christensen, E.A. Carter, Phys. Rev. B 58 (1998) 8050.
[13] L.E. Toth, Transition Metal Carbides and Nitrides, Academic Press, New York, 1971.
[14] B.G. Hyde, J.G. Thompson, R.L. Withers, in: R.W. Cahn, P. Haasen, E.J. Kramer, M.V. Swain (Eds.), Materials Science and Technology, vol. 11, VCH, New York, 1993, p. 1.
[15] R. Telle, in: R.W. Cahn, P. Haasen, E.J. Kramer, M.V. Swain (Eds.), Materials Science and Technology, vol. 11, VCH, New York, 1993, p. 119.
[16] F. Benesovsky, R. Kieffer, P. Ettmayer, in: Encyclopedia of Chemical Technology, vol. 15, John-Wiley, 1981, p. 871.
[17] D.D. Koelling, G.O. Arbman, J. Phys. F: Met. 5 (1975) 2041.
[18] O.K. Andersen, O. Jepsen, M. Sob, in: M. Yussouff (Ed.), Electronic Band Structure and its Applications, Springer Lecture Notes in Physics, 283, Springer, Berlin, 1987, p. 1.

[19] O.K. Andersen, Phys. Rev. B 12 (1975) 3060.
[20] J.-L. Calais, Adv. Phys. 26 (1977) 847, and references therein.
[21] A. Neckel, Int. J. Quantum Chem. 23 (1983) 1317, and references therein.
[22] J. Häglund, A.F. Guillermet, G. Grimvall, M. Körling, Phys. Rev. B 48 (1993) 11685.
[23] K.L. Hakansson, L.I. Johansson, P.L. Wincott, D.S.L. Law, Surf. Sci. 251/252 (1991) 108.
[24] P.A.P. Lindberg, P.L. Wincott, L.I. Johansson, A.N. Christensen, Phys. Rev. B 36 (1987) 4681.
[25] L.I. Johansson, Surf. Sci. Rep. 21 (1995) 177.
[26] A. Dominguez-Rodriguez, A.H. Heuer, in: L.C. Dufour et al. (Eds.), Surfaces and Interfaces of Ceramic Materials, Kluwer, 1989, p. 761.
[27] K.L. Hakansson, H.I.P. Johansson, L.I. Johansson, Phys. Rev. B 47 (1993) 16455.
[28] Y. Hwang, T. Aizawa, W. Hayami, S. Otani, Y. Ishizawa, S.-J. Park, Surf. Sci. 271 (1992) 299.
[29] S. Zaima, Y. Shibata, H. Adachi, C. Oshima, S. Otani, M. Aono, Y. Ishizawa, Surf. Sci. 157 (1985) 380.
[30] D.L. Price, B.R. Cooper, Phys. Rev. B 39 (1989) 4945.
[31] C. Oshima, M. Aono, T. Tanaka, S. Kawai, S. Zaima, Y. Shibata, Surf. Sci. 102 (1981) 312.
[32] A.M. Stoneham, M.M.D. Ramos, A.P. Sutton, Philos. Mag. A 67 (1993) 2221.
[33] S.V. Dudiy, J. Hartford, B.I. Lundqvist, Phys. Rev. Lett. 85 (2000) 1898.
[34] S.V. Dudiy, B.I. Lundqvist, Phys. Rev. B 64 (2001) 045403.
[35] J.P. Perdew, J.A. Chevary, S.H. Vosko, K.A. Jackson, M.R. Pederson, C. Fiolhais, Phys. Rev. B 46 (1992) 6671; J.P. Perdew, K. Burke, Y. Wang, Phys. Rev. B 54 (1996) 16533.
[36] M. Christensen, S.V. Dudiy, G. Wahnstrom, Phys. Rev. B 65 (2002) 045408.
[37] M.W. Chase (Ed.), NIST-JANAF Thermochemical Tables, 4th ed., AIP and ACS, 1998.
[38] R. Hultgren, P.D. Desai, D.T. Hawkins, M. Gleiser, K.K. Kelly, Selected Values of Thermodynamic Properties of Binary Alloys, ASM, Ohio, 1973.
[39] J.P. Perdew, A. Zunger, Phys. Rev. B 23 (1981) 511.
[40] G. Kresse, J. Furthmüller, Comput. Mater. Sci. 6 (1996) 15.
[41] D. Vanderbilt, Phys. Rev. B 41 (1990) 7892; G. Kresse, J. Hafner, J. Phys.: Condensed Matter 6 (1994) 8245.
[42] M. Methfessel, A.T. Paxton, Phys. Rev. B 40 (1989) 3616.
[43] C.S. Wang, B.M. Klein, H. Krakauer, Phys. Rev. Lett. 54 (1985) 1852.
[44] P. Villars, L.D. Calvert, Pearson's Handbook of Crystallographics Data on Intermetallics, ASM, Ohio, 1991.
[45] F.D. Murnaghan, Proc. Natl. Acad. Sci. 30 (1944) 2344.
[46] H.L. Brown, C.P. Kempter, Phys. Status Solidi 18 (1966) K21.
[47] A.G. Every, A.K. McCurdy (Eds.), Landolt-Börnstein—Group III Condensed Matter, 29 A, Springer-Verlag, Heidelberg, 1992, p. 576.
[48] R. Chang, L.J. Graham, J. Appl. Phys. 37 (1966) 10.
[49] H.G. Smith, in: D.H. Douglass (Ed.), Superconductivity in d- and f-Metals, AIP, New York, 1972.
[50] J.P. Perdew, A. Zunger, Phys. Rev. B 23 (1981) 5048.
[51] F.R. de Boer, R. Boom, W.C.M. Mattens, A.R. Miedema, A.K. Niessen, Cohesion in Metals, North-Holland, New York, NY, 1988.
[52] W.R. Tyson, W.A. Miller, Surf. Sci. 62 (1977) 267.
[53] L. Vitos, A.V. Ruban, H.L. Skriver, J. Kollar, Surf. Sci. 411 (1998) 186.
[54] D.R. Alfonso, J.A. Snyder, J.E. Jaffe, A.C. Hess, M. Gutowski, Phys. Rev. B 62 (2000) 8318.
[55] W.D. Callister Jr., in: Materials Science and Engineering, John Wiley and Sons, New York, 2000, p. 193.
[56] A. Christensen, E.A.A. Jarvis, E.A. Carter, in: R.A. Dressler (Ed.), Chemical Dynamics in Extreme Environments, in: C.Y. Ng (Ed.), Advanced Series in Physical Chemistry, 11, World Scientific, Singapore, 2001, p. 490.